Non-peer reviewed preprint submitted to EarthArXiv

Title	SCI-VIS*: Lightweight Visibility Tagging for Coastal Camera Monitoring*
Authors	Michael Reinwald[1], Ketron Mitchell-Wynne[1], Zane D'Amico[1], Mercedes Stringer[1], Benjamin Freeston[1]
Affiliation	[1]Surfline/Wavetrak, Inc., Huntington Beach, CA, USA
Corresponding author	Michael Reinwald <mreinwald@surfline.com>
ORCID	`https://orcid.org/0000-0001-8481-8392`
License	Creative Commons Attribution–NonCommercial 4.0 International (CC BY-NC 4.0)
Keywords	visibility classification; fog detection; image quality assessment; coastal cameras; surf-zone monitoring

SCI-VIS: Lightweight Visibility Tagging for Coastal Camera Monitoring

Michael Reinwald*[1], Ketron Mitchell-Wynne[1], Zane D'Amico[1], Mercedes Stringer[1], and Benjamin Freeston[1]

[1]Surfline/Wavetrak, Inc., Huntington Beach, CA, USA

Abstract

Automated assessment of imaging conditions is a necessary pre-processing step for any computer vision pipeline deployed on outdoor cameras subject to atmospheric variability. We describe SCI-VIS, a lightweight per-frame visibility classifier deployed within the Surfline Coastal Intelligence (SCI) pipeline. The Surfline coastal-camera network spans ∼1,200 cameras worldwide. SCI-VIS tags each incoming frame with one or more concurrent conditions: *Clear*, *Glare*, *Fog*, *Rain/Blur*, *Hazy*, and *Dark*. The classifier combines a compact handcrafted image-feature representation with a gradient-boosted tree classifier, deployed CPU-only at the per-rewind cadence of the SCI archive. A multi-rank label scheme allows each frame to carry multiple simultaneous condition tags. The model is trained on 12,435 frames from a 15,543-frame manually-labelled dataset drawn from 595 cameras (a subset of the full network). On the 3,108-frame held-out test set it achieves 92.9% primary-label accuracy and 87.3% exact multi-rank match accuracy, with strong performance on the dominant conditions (F1 = 0.96 for *Clear*, 0.90 for *Glare*, 0.87 for *Fog*) and weaker recall on the rarest conditions (F1 = 0.46 for *Hazy*); because the train/test split is at the frame level, these figures are in-distribution estimates over the operational camera distribution the model is deployed against. Confusion analysis shows that the residual error is biased toward the majority *Clear* class—a direct consequence of class imbalance (74% *Clear*)—so misclassifications fall on borderline degraded frames and are addressable through class-weighted training or threshold adjustment. The model requires no GPU and is invoked once per rewind (the fixed-duration video segment forming the atomic unit of the camera archive), making the ∼1.8 s per-frame CPU cost operationally negligible.

Keywords: visibility classification, fog detection, image quality assessment, coastal cameras, surf-zone monitoring

1 Introduction

Outdoor camera networks deployed for environmental monitoring must contend with a continuous spectrum of atmospheric and optical degradation: sea fog rolling in over the water, sun glare saturating the sensor, rain or condensation blurring the lens, haze reducing contrast, or darkness falling outside operating hours. For downstream computer vision tasks—breaking-wave-height estimation, object detection, segmentation—these conditions represent noise sources that can corrupt measurements or trigger false positives. A fast, reliable method for tagging each incoming frame with its prevailing visibility conditions is therefore a foundational module for any production-grade coastal CV pipeline. Because atmospheric visibility is spatially heterogeneous—coastal fog in particular is patchy, often obscuring one camera while a neighbour kilometres away stays clear [Rauschenbach et al., 2026]—this assessment must be made per camera from the imagery itself, rather than inferred from the nearest weather station.

Surfline operates one of the world's largest networks of coastal surf cameras (∼1,200 cameras worldwide), and the Surfline Coastal Intelligence (SCI) pipeline runs downstream computer-vision modules on imagery from this network. The training set used to fit the visibility classifier described in this paper was assembled from frames captured at 595 of these cameras (see Section 3). Each camera streams video continuously to a processing backend where downstream modules estimate breaking-wave-height, track breaking events, count recreational users, and generate ocean-condition reports — all resting on an upstream semantic-segmentation stage. The quality of these estimates depends on the imaging conditions at capture time: a fog-obscured scene yields unreliable breaking-wave-height measurements, heavy glare corrupts edge detection, and rain on the lens degrades every pixel. SCI-VIS, the subject of this paper, produces a per-rewind visibility label that the SCI pipeline's aggregation layer uses to exclude degraded rewinds from reported aggregates. It does not gate the inference of the downstream ML models themselves — those run on every rewind — but it is what makes aggregated downstream outputs robust to atmospheric and optical degradation.

Deep learning approaches to outdoor weather and visibility classification have achieved high accuracy on benchmark datasets [Lu et al., 2014, Yang et al., 2023], but carry significant inference costs that make them impractical for deployment at scale without dedicated GPU hardware at every node. Feature-engineering approaches [Hautière et al., 2006, Bronte et al., 2009] offer a compelling alternative when the discriminating signals are well-understood and the deployment cost budget rules out per-frame GPU inference.

This paper describes SCI-VIS, a production classifier that has been deployed across the Surfline camera network. The model's design philosophy is to extract a compact set of physically-motivated, computationally cheap features and to classify them with a gradient-boosted tree ensemble—requiring no GPU at inference time and no change to the feature pipeline or model architecture as the camera network grows. The model operates in a *multi-rank* mode, allowing each frame to carry multiple simultaneous condition labels, reflecting the real-world co-occurrence of visibility conditions (e.g. fog and glare at sunrise).

This paper documents a deployed system and characterises its single-frame performance on a held-out test set drawn from the same operational camera distribution. The value is in the combination: a coastal-domain training set spanning a large camera network, a multi-rank labelling scheme that captures the real-world co-occurrence of conditions, and operation as a CPU-only component of a larger network-scale CV pipeline. We make the resulting performance profile available to other groups working on coastal-camera analytics. Comparison against next-generation methods (CLIP-style zero-shot scene tagging, vision–language-model condition assessment, deep CNN visibility classifiers) and against external ground truth (e.g. co-located weather stations, visibility sensors, human spotter logs) is out of scope here and left to future work.

Specifically, the contributions of this paper are:

1. A description of the handcrafted feature representation — combining 2D Fourier power spectra, RGB histograms, Local Binary Patterns, Canny edge statistics, and Laplacian variance — and a physical motivation for each group's discriminative value.

2. A multi-rank label scheme that allows each frame to carry multiple simultaneous condition tags, encoding the real-world co-occurrence of visibility conditions.

3. A curated dataset of 15,543 manually-labelled frames from 595 cameras, together with the operational training and evaluation pipeline.

4. Quantitative evaluation of per-class and multi-rank accuracy, confusion analysis, and feature importance, characterising where the model succeeds and where class imbalance limits recall for rare conditions.

The remainder of the paper is structured as follows. Section 2 surveys related work on visibility estimation and outdoor scene classification. Section 3 describes the dataset and labelling methodology. Section 4 presents the feature extraction pipeline and classifier. Section 5 reports evaluation results. Section 6 discusses limitations and directions for future work. Section 7 concludes.

2 Related Work

2.1 Outdoor scene visibility and weather classification

The problem of automatically classifying atmospheric visibility from single images has a long history in computer vision. Early work by Hautière et al. [2006] used gradient analysis in road scenes to estimate the visibility distance under fog. Image-based fog detection methods typically exploit the observation that fog attenuates contrast and reduces the scene's dynamic range, motivating histogram-based and edge-based features [Hautière et al., 2006, Bronte et al., 2009].

More recently, deep convolutional networks have been applied to weather and degradation classification. Lu et al. [2014] combined a CNN with weather-specific cues in a collaborative learning framework for two-class outdoor weather classification, and Yang et al. [2023] proposed a multitask CNN cascade (VENet) that jointly classifies fog level and estimates fog visibility distance on expressway surveillance imagery. These convolutional classifiers achieve high accuracy on in-distribution benchmarks but require GPU compute at inference time, which is a significant cost when the same classifier must run continuously across a large fleet of streaming cameras.

2.2 Fourier-based texture analysis

The two-dimensional power spectrum of a natural image encodes information about the spatial frequency content and directionality of texture, making it a useful probe of atmospheric attenuation. Field [1987] established that the power spectra of natural images follow an approximate $1/f^{\alpha}$ fall-off (with $\alpha \approx 2$ for the 2D radially-averaged spectrum), and deviations from this slope are diagnostic of blur, noise, and atmospheric haze. In the visibility context, fog attenuates high spatial frequencies more strongly than low ones, shifting the spectral slope; glare introduces a DC offset through saturation; and rain generates characteristic high-frequency noise.

2.3 Local Binary Patterns

Local Binary Patterns (LBP), introduced by Ojala et al. [2002], encode the local texture structure of an image by comparing each pixel to its circular neighbourhood and assembling the comparison bits into a histogram. The "uniform" variant [Ojala et al., 2002] retains patterns with at most two bitwise transitions, giving a compact descriptor. LBP histograms have been widely used for texture classification in outdoor scenes [Pietikäinen et al., 2011], and are particularly effective at distinguishing smooth foggy or hazy scenes (dominated by low-entropy uniform patterns) from clear scenes with rich edge structure.

2.4 Gradient-boosted trees for image features

XGBoost [Chen and Guestrin, 2016] and its variants have demonstrated strong performance on tabular and structured-feature problems, particularly when the feature space is compact (tens to hundreds of dimensions) and the signal-to-noise ratio is high. For outdoor scene classification tasks where discriminative features can be hand-engineered, gradient-boosted ensembles offer several practical advantages over deep networks: fast training, built-in feature importance scores, and interpretable outputs. Daneshvari et al. [2023] applied a similar combination of handcrafted texture features (LBP and GLCM) and XGBoost to asphalt pavement raveling detection.

2.5 Marine and coastal visibility estimation

Camera-based visibility estimation in marine environments is a specific and challenging sub-problem. Sea fog is common in coastal regions due to advection of warm moist air over cold ocean surfaces [Lewis et al., 2003], and its optical properties differ from continental fog. Bae et al. [2019] estimated visibility distance from coastal CCTV imagery using a dark-channel-prior transmission map combined with a distance-map calibration, evaluated at three Korean ports.

Most directly related to the present work, Rauschenbach et al. [2026] independently applied image-based fog detection to the same class of imagery: five of their six Oregon-coast camera sites are Surfline cameras drawn from the network studied here. They compute the nine Fog-Aware Statistical Features of Choi et al. [2015]—among them local contrast, image entropy, colourfulness, and the dark-channel prior—over three horizontal image strips and classify fog presence with a Gaussian-process classifier, reaching a fog F1 of 0.87. Their formulation is binary (fog / no fog), tied to World Meteorological Organization visibility thresholds, and validated against a forward-scatter visibility sensor at a nearby airport; it is complementary to the multi-condition, network-scale tagging task addressed here. We return to this comparison in Sections 5 and 6.

Low-light and nighttime conditions present additional challenges due to the fundamentally different appearance of atmospheric scattering under reduced illumination. Our approach addresses all these conditions in a unified framework, relying on the same compact feature vector across diurnal and seasonal variation.

3 Data

3.1 Dataset overview

The training dataset consists of 15,543 still frames extracted from the Surfline camera network, drawn from 595 cameras (a subset of the ∼1,200-camera network) across diverse geographic locations spanning the continental United States, Hawaii, Indonesia, Australia, and Europe. Frames were collected across all seasons and times of day. Figure 1 summarises the per-condition frame counts; the "primary-label" class is the condition the annotator judged to occupy the largest share of the surf zone in each frame, and the labelling schema that produces it is described in Section 3.3.

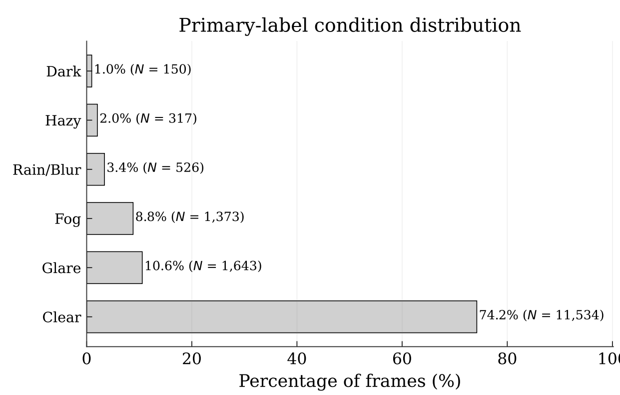

Figure 1: Distribution of primary-label visibility conditions across the training and test sets (combined). The dataset is strongly imbalanced toward *Clear* frames, reflecting the relative frequency of good-visibility conditions in practice.

3.2 Class taxonomy

The six visibility conditions are defined as follows:

- **Clear (0):** Good visibility, no atmospheric or optical artefacts. The horizon and surf zone are clearly resolved.
- **Glare (1):** Sun glare on the sensor or water surface, causing partial or full saturation and loss of contrast in the affected region.

- **Fog (2):** Low-lying or advection fog obscuring the horizon and distant surf, reducing contrast and blurring distant features.
- **Rain/Blur (3):** Rain droplets on the lens, optical blur, or precipitation visible in the scene, reducing image sharpness.
- **Hazy (4):** Atmospheric haze or sea spray reducing contrast without complete obscuration. Distinguished from *Fog* by the presence of a discernible but degraded horizon.
- **Dark (5):** Low-light conditions (pre-dawn, post-dusk, overcast night) that result in reduced dynamic range and elevated sensor noise. Distinct from the un-interpretable nighttime frames excluded by the -1 flag described in Section 3.3.

Figure 2 shows representative frames for each condition.

3.3 Annotation methodology

Frames are labelled in Encord, our managed annotation platform, by a small pool of trained annotators following a written labelling guide. The guide frames the task explicitly in terms of the downstream consumers: visibility labels are used to flag frames where the segmentation and object-detection models are likely to be degraded *within the surf zone*, so annotators are instructed to assess each frame's visibility conditions over the surf-zone region rather than the full image.

The schema is *multi-rank*: each frame carries up to three ordered labels, drawn from the six conditions of Section 3.2 and stored in the PrimaryVisibility, SecondaryVisibility, and (rarely) TertiaryVisibility slots. When two or more conditions co-occur in distinct parts of the surf zone, annotators rank them by the fraction of surf-zone area each condition affects: the condition occupying the largest share is the primary label, the next largest the secondary, and so on. A frame whose surf zone is roughly 70% clear water with glare covering the remaining 30%, for example, is labelled Primary=*Clear*, Secondary=*Glare*; a single-condition frame uses only the primary slot. Frames that do not fit any class or are otherwise ambiguous are flagged for review rather than guessed.

Figure 3 reproduces the canonical multi-rank cases from the labelling guide. The reversed two-rank pairs (e.g. *Clear, Glare* vs. *Glare, Clear*) make the surf-zone-area convention concrete: the same pair of conditions receives opposite rank orderings depending on which condition affects more of the surf zone. The bottom row shows the comparatively rare cases where a third rank is required.

A separate *nighttime exclusion* flag (-1) is applied to frames that are too dark to classify reliably at all—deep nighttime or severely underexposed scenes where neither segmentation nor detection would be expected to operate. These frames are excluded from training and evaluation, and are distinct from the *Dark* class above, which covers low-light but still interpretable conditions such as pre-dawn and post-dusk.

3.4 Train/test split

The dataset is split 80/20 (train/test) using a random permutation. The split is at the individual-frame level: cameras that appear in training may also appear in the test set. This matches the operational regime in which the model is deployed. When a new camera is added to the network, a small batch of frames from that camera is labelled and folded into the training set before the model is retrained, so the production model is never asked to generalise to a wholly unseen camera in zero-shot fashion. The frame-level split therefore measures the quantity that matters operationally—accuracy on new frames from the camera distribution the model is trained against—rather than a zero-shot generalisation bound that the deployment process is designed to avoid. See Section 6 for further discussion.

4 Methods

4.1 Region of interest

Each frame is resized to a fixed resolution before feature extraction. No further spatial cropping is applied by default; the full frame is used. An optional horizon-guided crop is available (using the SCI pipeline's upstream semantic segmentation model to detect the horizon and shoreline positions) but was not used in the configuration evaluated here, as it did not improve accuracy on the held-out test set and added inference latency.

This introduces a deliberate asymmetry between the label and the feature support: annotators judge visibility over the surf-zone region (Section 3.3), whereas the feature vector summarises the whole frame. We retain the full-frame representation both because the surf-zone crop did not improve held-out accuracy and because whole-frame statistics (sky luminance, horizon contrast, global texture) are themselves informative of the conditions affecting the surf zone. The residual cost is that a degradation confined to a small part of the surf zone within an otherwise clear wide frame can be diluted in the global features, which is consistent with the *Hazy*→*Clear* leakage analysed in Section 6.

4.2 Feature extraction

The model operates on a compact handcrafted feature vector composed of five feature groups, described below. Each group was selected because the underlying

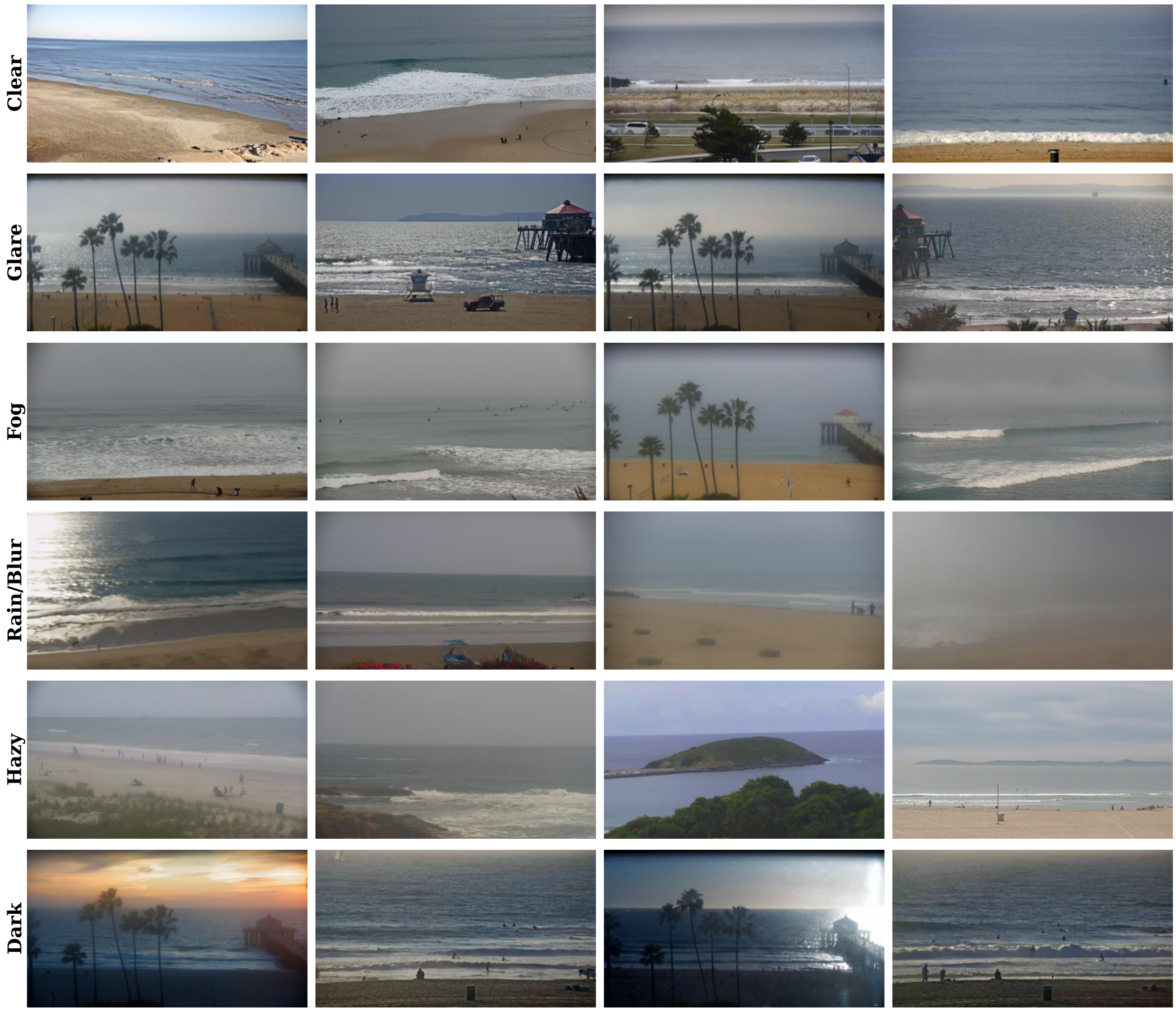

Figure 2: Representative frames for each of the six visibility conditions. Each row shows four frames from different cameras and locations illustrating within-class variation. *Clear* frames span diverse lighting, wave conditions, and camera orientations. *Glare* frames range from mild specular highlights to full sensor saturation. *Fog* frames include both dense advection fog and patchy coastal fog. *Rain/Blur* includes lens rain, streaking, and optical defocus. *Hazy* frames show reduced contrast without complete horizon obscuration. *Dark* frames include pre-dawn, deep overcast, and post-dusk conditions.

image statistic is sensitive to one or more of the optical degradations the classifier must distinguish (atmospheric scattering, sensor saturation, defocus, low light); we do not claim a one-to-one mapping between feature groups and visibility classes, and the per-class attribution required to make such claims (e.g. SHAP, group-wise ablation) is left to future work (Section 6). Specific bin counts, kernel parameters, and normalisation constants are operational tuning artefacts and are not disclosed.

4.2.1 Two-dimensional power spectrum

The 2D angular power spectrum [Field, 1987] of an image is computed by binning the squared amplitude of its Fourier transform into a small number of log-spaced annuli in frequency space, and computed separately for each of the R, G, and B channels.

The radially-averaged power spectrum of natural images approximately follows a $1/f^{\alpha}$ fall-off [Field, 1987], and atmospheric scattering acts as a low-pass filter that preferentially attenuates high spatial frequencies; the distribution of energy across log-spaced frequency bins

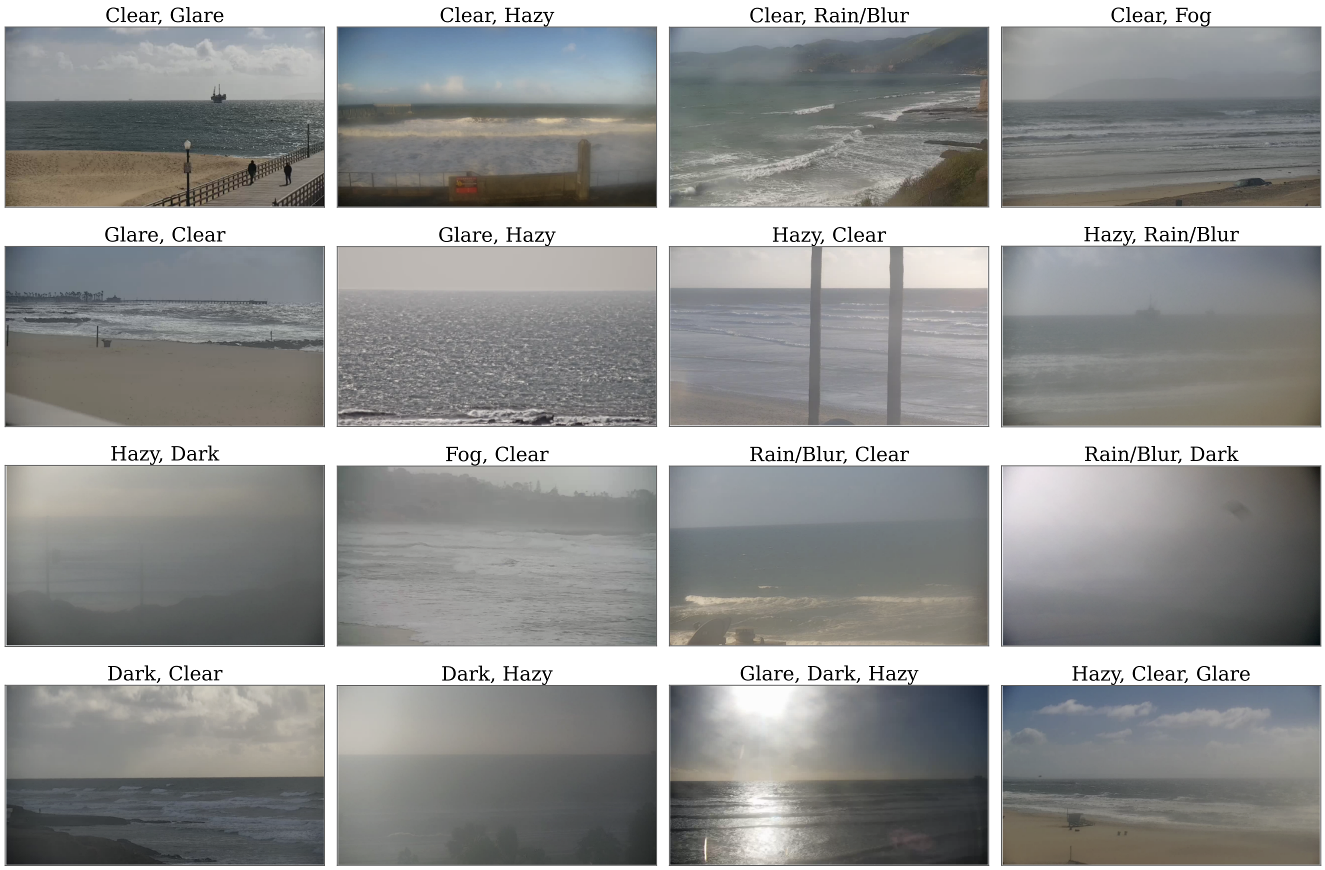

Figure 3: Canonical multi-rank labelling examples reproduced from the annotator guide. Each panel's title gives the rank order (*Primary, Secondary* or *Primary, Secondary, Tertiary*). The reversed two-rank pairs—*Clear, Glare*/*Glare, Clear*; *Hazy, Clear*/*Clear, Hazy*; *Fog, Clear*/*Clear, Fog*; *Rain/Blur, Clear*/*Clear, Rain/Blur*; *Dark, Hazy*/ *Hazy, Dark*—make the surf-zone-area ranking convention concrete: the same pair of conditions receives opposite labels depending on which condition affects more of the surf zone. The bottom row shows the rare cases where a third rank is required.

is therefore expected to carry signal about scattering-driven degradation. Power-spectrum bins do appear in the top of the aggregate feature-importance ordering reported in Section 5.

4.2.2 RGB channel histograms

Per-channel intensity histograms are computed over the full frame and normalised to yield an intensity probability mass function. The histogram captures the global luminance and colour distribution of the frame, which can be expected to vary with illumination level and sensor saturation. We do not assign specific histogram shapes to specific visibility classes here; what we observe empirically (Section 5) is that several histogram bins appear in the top of the aggregate feature-importance ordering.

4.2.3 Local Binary Pattern histogram

The Local Binary Pattern (LBP) [Ojala et al., 2002] describes local texture by comparing each pixel to its circular neighbourhood and encoding the comparisons as a binary string. Using the "uniform" variant, the resulting histogram provides a compact summary of image texture and is computed on a denoised grayscale version of the frame to suppress sensor noise before pattern extraction.

LBP histograms are an established texture descriptor for outdoor-scene classification [Pietikäinen et al., 2011] and provide a low-cost summary of local image structure that is complementary to the global statistics captured by the histogram and power-spectrum features. Several LBP histogram bins rank near the top of the aggregate feature-importance ordering reported in Section 5.

4.2.4 Edge statistics

Two complementary edge metrics are extracted from a Canny edge map [Canny, 1986]: the mean of the binary edge map (μ_{edge}, measuring the fraction of pixels classified as edges) and its standard deviation (σ_{edge}). The detector is operated in a regime that produces a sparse, high-confidence edge map robust to JPEG compression artefacts common in the surf-camera stream, so that the edge density signal tracks genuine scene structure rather than compression ringing. Edge density is a classical correlate of image-quality degradation under contrast loss and blur [Hautière et al., 2006], and the Canny edge density emerges as the single highest-ranked feature in the aggregate importance analysis (Section 5).

4.2.5 Laplacian variance

The variance of the Laplacian operator applied to the frame is used as a classical measure of image sharpness [Pertuz et al., 2013] and provides a global summary of high-frequency content that is complementary to the localised Canny edge statistics.

4.3 Multi-rank label encoding

Each training frame carries one or more condition labels. To encode these as a single target class for the gradient-boosted classifier, label combinations are treated as distinct class strings. A frame labelled *Clear+Glare* is mapped to the string "01" and a frame labelled *Fog* alone is mapped to "2". All unique combinations observed in the full labelled dataset are enumerated and assigned integer class IDs.

This encoding preserves full label information during training. The combination space is highly sparse: a small number of common combinations dominate the dataset, while many appear in fewer than ten training examples. For evaluation purposes, the primary (first-listed) condition is extracted from the predicted class string—this is the same condition that the annotator stored in the PrimaryVisibility slot (Section 3.3)—reducing the comparison to a standard 6-class problem.

4.4 Gradient-boosted classifier

A multi-class gradient-boosted tree classifier [Chen and Guestrin, 2016] is trained on the multi-rank class encoding with a probabilistic output objective; the final class is determined by argmax over the output distribution.

5 Results

5.1 Classification accuracy

Table 1 reports accuracy metrics on the held-out test set (3,108 frames). The model achieves 87.3% exact-match accuracy on multi-rank class strings and 92.9% primary-label accuracy, where only the primary (first-listed) predicted condition is compared to the primary ground-truth condition. The gap between these two figures—approximately 5.6 percentage points—is the rate at which the model identifies the primary condition correctly but omits or reorders a secondary condition. That the model nonetheless reproduces the full multi-rank string exactly on 87.3% of frames shows it is capturing co-occurrence structure rather than only the dominant condition.

As baselines, always predicting the majority class (*Clear*) yields 74% primary-label accuracy, and an L2-regularised multinomial logistic regression trained on the same standardised features against the same 6-class primary-label targets achieves 87.7%. The 5.2 percentage-point improvement of the gradient-boosted classifier over logistic regression indicates that the non-linear interactions captured by tree ensembles add meaningful discriminative power beyond what is available in the raw feature magnitudes.

Table 1: Summary accuracy metrics on the held-out test set.

Metric	Value
Majority-class baseline (primary-label)	74%
Logistic regression (primary-label)	87.7%
SCI-VIS (primary-label)	92.9%
SCI-VIS (exact multi-rank)	87.3%
Test set size (frames)	3,108
Training set size (frames)	12,435

5.2 Per-class performance

Table 2 and Figure 4 report per-class precision, recall, and F1 score computed on primary-label predictions. Performance varies substantially across classes, largely tracking their prevalence in the training data. *Clear* dominates the dataset (74% of frames) and is classified with high precision (0.94) and very high recall (0.98). At the other extreme, *Hazy* (2.0% of frames) has the weakest F1 score (0.46), driven primarily by poor recall (0.35)—the model correctly identifies only one in three genuinely hazy frames. *Rain/Blur* (3.4% of frames) similarly shows lower precision (0.78) and recall (0.69) relative to the more common conditions. *Glare*, *Fog*, and *Dark* all achieve F1 scores above 0.87 despite representing 10.6%, 8.8%, and 1.0% of the dataset respectively.

Table 2: Per-class precision, recall, and F1 score on primary-label predictions. N is the number of test frames with that primary label. The 95% bootstrap CI on recall (2,000 resamples) is shown for each class; it is widest for the minority classes, where small N makes the point estimates least reliable.

Class	Precision	Recall	F1	N	95% CI (recall)
Clear	0.94	0.98	0.96	2,290	[0.97, 0.98]
Glare	0.94	0.86	0.90	329	[0.82, 0.89]
Fog	0.90	0.84	0.87	297	[0.80, 0.88]
Rain/Blur	0.78	0.69	0.74	98	[0.60, 0.79]
Hazy	0.67	0.35	0.46	62	[0.24, 0.48]
Dark	0.96	0.81	0.88	32	[0.67, 0.94]

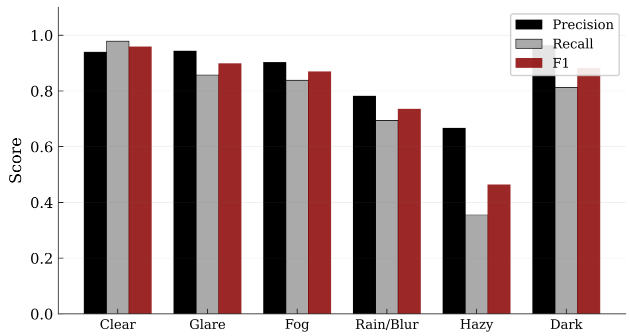

Figure 4: Per-class precision (black), recall (grey), and F1 score (dark red) for primary-label prediction on the test set. Performance degrades for minority classes: *Hazy* (2.0% of data) has the lowest recall (0.35) and *Rain/Blur* (3.4% of data) the second-lowest. The three numerically dominant classes—*Clear*, *Glare*, and *Fog*—all achieve F1 $>$ 0.87.

It is notable that Rauschenbach et al. [2026], using an entirely independent implementation—a Gaussian-process classifier on the Fog-Aware Statistical Features of Choi et al. [2015], evaluated on a subset of the same camera network—report an identical fog F1 of 0.87. That two classifiers built on disjoint feature sets (their FADE features versus our Fourier/LBP/edge representation) and different learning algorithms converge on the same fog-detection performance suggests that $\approx$0.87 F1 reflects a practical ceiling for handcrafted-feature classical machine learning on this class of coastal imagery, rather than an artefact of any particular feature or model choice.

5.3 Confusion matrix

Figure 5 shows the confusion matrix on primary-label predictions normalised by true class (row). The dominant off-diagonal pattern is *degraded condition* $\rightarrow$ *Clear*: 48% of *Hazy* frames are predicted as *Clear*, 22% of *Rain/Blur* frames, 15% of *Fog* frames, 14% of *Glare* frames, and 12% of *Dark* frames. This asymmetric pull toward the majority class is a direct consequence of the severe class imbalance in the labelled dataset (74% *Clear*) and reflects the fact that many degraded frames share sufficient feature overlap with typical clear scenes to fall below the effective decision boundary.

Secondary confusion patterns are less prominent but physically interpretable: *Rain/Blur* is confused with *Fog* in 6% of cases (both suppress edge density), and 13% of *Hazy* frames are misclassified as *Rain/Blur* (both reduce local contrast and LBP entropy). Notably, *Fog/Hazy* cross-confusion is modest—only 3% of *Hazy* frames go to *Fog*—contradicting the intuition that these two classes form the primary confusion axis. The more pressing issue is that both conditions tend to be predicted as *Clear* when the degradation is mild.

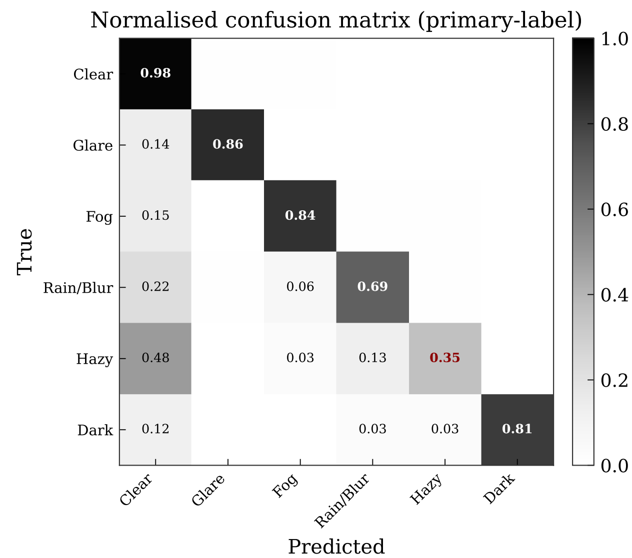

Figure 5: Row-normalised confusion matrix for primary-label predictions. The dominant off-diagonal signal is a pull toward *Clear* (the majority class at 74% of the labelled dataset), strongest for *Hazy* (48% misclassified as Clear) and *Rain/Blur* (22%). Diagonal entries are correct predictions.

5.4 Feature importance

Figure 6 shows the top features ranked by mean gain (class-agnostic; aggregated over all output classes). The single highest-ranked feature—the top *Edge / Laplacian* bar in Figure 6—is the Canny edge-density statistic, followed by several LBP histogram bins. RGB-histogram features are the most numerous of the remaining top-20 entries, with power-spectrum bins also represented. Each of the five feature families is represented in the top 20, indicating that the classifier's decisions draw on all of them rather than relying disproportionately on any single group. The mean-gain ranking is class-agnostic and does not by itself attribute particular features to particular classes; per-class attributions would require a class-conditional importance analysis (e.g. SHAP), which is left to future work.

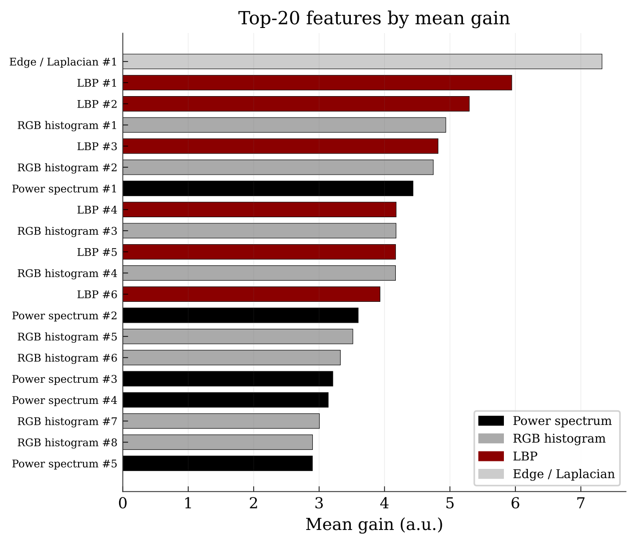

Figure 6: Top features by mean gain, coloured by feature group (power spectrum: black; RGB histogram: grey; LBP: dark red; edge/Laplacian: light grey). Within-family labels are anonymised (e.g. "LBP #1, #2, ...") so that bars convey relative ordering of feature *families* rather than specific feature indices. The ranking is class-agnostic.

5.5 Qualitative examples

Figure 2 shows representative frames for each condition.

6 Discussion

6.1 Class imbalance as the dominant error driver

The most important finding from the confusion analysis is that the dominant failure mode is not inter-class ambiguity between visually similar conditions, but rather a systematic pull toward the majority class. Nearly half of all *Hazy* frames (48%) are predicted as *Clear*, as are 22% of *Rain/Blur* frames, 15% of *Fog* frames, 14% of *Glare* frames, and 12% of *Dark* frames. This pattern is consistent with the dataset distribution: *Clear* accounts for 74% of all labelled frames. When the feature overlap between a mildly degraded frame and a typical clear frame is non-negligible, the classifier resolves the ambiguity by defaulting to the prior-weighted majority class.

This has a direct operational implication. The model's output is consumed by the SCI pipeline's downstream aggregation stages, which use it to exclude degraded rewinds from reported wave-height, shoreline, and object-count outputs. The error here is bounded and well-characterised rather than catastrophic: the model classifies the dominant *Clear* condition with F1 = 0.96 across the 74% of frames it represents, and the residual leakage is concentrated in the most transitional condition (*Hazy*, 48% of which is read as *Clear*) while the more distinct degradations are largely retained (only 15% of *Fog* and 12% of *Dark* frames leak through). The remedy is well understood and tunable: addressing the class imbalance in training (resampling, class-weighted loss) or lowering the decision threshold for non-Clear predictions both raise degraded-frame recall, and either can be set to the error tolerance of the specific downstream consumer.

This conservative bias—higher precision than recall on the degraded classes, with marginal frames preferentially read as *Clear*—is not unique to our implementation. Rauschenbach et al. [2026] report the same tendency for their Gaussian-process fog classifier evaluated on a subset of the same camera network: their model consistently under-predicts fog relative to human labels, yielding higher precision than recall. That two independent handcrafted-feature classifiers, built on disjoint feature sets, share this failure mode suggests it is a property of the feature class and the underlying class imbalance rather than of our specific training data or hyperparameters.

6.2 The Hazy class requires special attention

Hazy is the weakest class by a wide margin (F1 = 0.46, recall = 0.35). Two factors plausibly compound to produce this. First, the class is severely underrepresented (255 training frames after the split, 2.1% of the training set). Second, the class is definitionally transitional: a frame labelled *Hazy* represents intermediate atmospheric attenuation that exists on a continuum with both *Clear* (at the mild end) and *Fog* (at the severe end), so a non-trivial fraction of borderline frames is expected to be ambiguous to any single-frame classifier — including a human annotator. We do not attempt to characterise the feature-space behaviour of the *Hazy* class quantitatively here; doing so requires the class-conditional attribution analysis discussed below and is left to future work.

The 13% of *Hazy* frames that are predicted as *Rain/Blur* are a secondary confusion that we record as an empirical observation but do not attempt to attribute to a specific feature-level mechanism in this paper.

Two feature-level extensions are promising avenues for improving *Hazy* and *Fog* recall specifically. First, the dark-channel prior [He et al., 2011, Bae et al., 2019]—the canonical haze descriptor in the dehazing literature, and one of the Fog-Aware Statistical Features used by Rauschenbach et al. [2026], but absent from our current feature set—directly measures the atmospheric-scattering signal that distinguishes hazy and foggy scenes from clear ones. Second, spatially-resolved features that contrast the horizon band against the foreground (as in the three-strip decomposition of Rauschenbach et al. [2026]) exploit the fact that fog and haze attenuate distant parts of the scene more than near ones; our current full-frame features discard this vertical structure.

6.3 Feature group contributions in context

The aggregate feature-importance ranking shows that each of the five feature families is represented in the top of the ordering, with the Canny edge density the single highest-ranked feature and several LBP histogram bins also among the top entries; power-spectrum and RGB-histogram features fill out the remainder. This is a class-agnostic mean-gain ranking, so it tells us only that the classifier draws on all five feature families when partitioning the joint input–output space; it does not by itself license claims about which feature group carries the signal that distinguishes any particular pair of classes. A class-conditional attribution analysis (e.g. SHAP, ablation by feature group) would be required to support such claims and is left to future work.

6.4 Inference cost and operational deployment

The full feature extraction pipeline takes approximately 1.8 s per frame on a single CPU core. This makes the model unsuitable for per-frame real-time inference at typical camera frame rates (10–30 fps), but well-suited to the sampling strategy used in production: the classifier is invoked once per *rewind*—the fixed-duration video segment ($\sim$10 minutes) that forms the atomic unit of the SCI pipeline archive. The first frame of each rewind is assessed for visibility, and the resulting label is applied to the entire segment before any downstream CV modules are invoked. At this cadence, one classification per rewind, the 1.8 s per-frame CPU cost is entirely negligible.

6.5 Limitations

Class imbalance. The strong skew toward *Clear* frames in the labelled data (74%) directly reduces recall for minority conditions. Collecting additional labelled data for *Hazy* (255 training frames, 2.1% of the training set) and *Dark* (118 training frames, 1.0%), or applying class-weighted training, would likely yield the largest single improvement in operational utility.

Evaluation regime and unseen cameras. The train/test split is at the frame level; cameras that appear in training also appear in the test set. This is a deliberate match to how the model is deployed: when a new camera is brought online, a handful of frames from that camera are labelled in Encord and added to the training set before the next retraining cycle, so the production model is never asked to classify an unseen camera in zero-shot fashion. Reported accuracy is therefore an *in-distribution* estimate over the operational camera distribution, which is the quantity the deployment process is designed to optimise. A separate camera-holdout evaluation would answer a different question—zero-shot generalisation to wholly unseen hardware and locations—which is not the regime SCI-VIS operates in and is not a goal of the system. We do note that cameras at locations prone to specific conditions (coastal fog belts, high-glare tropical beaches) benefit from having site-representative frames in the training set, which the labelling-on-onboarding workflow is designed to provide.

Condition definitions. The boundary between *Hazy* and lightly *Foggy*, or between *Dark* and very overcast *Clear*, is subjective and annotator-dependent. The dataset was labelled by a small team with established guidelines but without formal inter-annotator agreement measurement. Formally quantifying this ambiguity—for instance via the multi-labeler consensus approach of Rauschenbach et al. [2026], who assigned a subset of images to five additional annotators to measure labelling uncertainty—would help bound the irreducible disagreement in the transitional classes and separate it from model error.

Single-frame sampling per rewind. In deployment the classifier is run on the first frame of each rewind and the resulting label is applied to the entire $\sim$10-minute segment, as described above. This assumes the first frame is representative of the segment, which holds well for slowly varying conditions (fog, haze, darkness) but less so for transient or onsetting conditions such as glare, which can develop within a single rewind. Sampling several frames per rewind and aggregating their labels, or re-assessing when frame-to-frame feature changes are large, would reduce this risk at modest additional cost.

No temporal context. The model treats each frame independently. In practice, visibility transitions are smooth and temporally correlated. A model that incorporates a short rolling window of feature vectors—or uses the previous frame's prediction as a prior—could substantially reduce transient misclassifications, particularly for the *Hazy* class where single-frame evidence is ambiguous.

7 Conclusion

We have described SCI-VIS, a deployed per-frame visibility classifier for the Surfline coastal camera network. The model combines a compact handcrafted feature representation—drawing on 2D Fourier power spectra, RGB histograms, Local Binary Patterns, Canny edge statistics, and Laplacian variance—with a gradient-boosted tree classifier trained on 15,543 manually-labelled frames from 595 cameras. A multi-rank label scheme accommodates the co-occurrence of visibility conditions and distinguishes *Clear*, *Glare*, *Fog*, *Rain/Blur*, *Hazy*, and *Dark*.

On the held-out test set the model achieves 92.9% primary-label accuracy and 87.3% exact multi-rank match accuracy. Performance is strong for the three dominant classes (*Clear*: F1 = 0.96; *Glare*: F1 = 0.90; *Fog*: F1 = 0.87) but weaker for the two rarest conditions (*Hazy*: F1 = 0.46; *Rain/Blur*: F1 = 0.74). Confusion analysis shows that the residual error is biased toward the majority *Clear* class: 48% of *Hazy* frames, 22% of *Rain/Blur* frames, and 15% of *Fog* frames are predicted as *Clear*. This is a direct consequence of the 74% *Clear* class prevalence in the labelled dataset; because the leakage is concentrated in borderline degraded frames while the dominant conditions are classified accurately, the known remedies—class-weighted training and threshold adjustment—offer a clear path to further gains. The aggregate feature-importance ranking shows all five feature families represented in the top of the ordering, with edge and texture features ranked highest; class-conditional attribution is left to future work.

The model requires no GPU at inference time and is invoked once per rewind—the fixed-duration video segment that forms the atomic unit of the camera archive—making the $\sim$1.8 s per-frame CPU cost operationally negligible. Its output is consumed by the SCI pipeline's downstream aggregation stages, which use it to exclude degraded rewinds from reported aggregates in wave-height estimation, object detection, and surf-condition assessment across the Surfline camera network. SCI-VIS does not gate the inference of those modules — they run on every rewind — but it is what makes their aggregated outputs robust to atmospheric and optical degradation. This paper provides a documentary description of the operational system—its feature families, training dataset, evaluation protocol, and characteristic failure modes—and identifies class imbalance as the primary lever for future improvement.

Author disclosure

B. Freeston, a co-author of this paper, is the named inventor on US Patent 10,891,481 B2 [Freeston, 2021], assigned to Surfline/Wavetrak, Inc., which discloses the broader automated ocean-sensing framework within which SCI-VIS was developed.

Competing interests

All authors are employees of Surfline/Wavetrak, Inc., which develops and commercially operates the SCI pipeline and the SCI-VIS classifier described in this paper.

Data and code availability

The training dataset, model weights, exact feature-extraction parameters, and training hyperparameters are proprietary and are not released. The model family, feature-group composition, evaluation protocol, and failure-mode characterisation described in this paper characterise the operational system as deployed.

References

Tae Wuk Bae, Jin Hyun Han, Kuk Jin Kim, and Young Taeg Kim. Coastal visibility distance estimation using dark channel prior and distance map under sea-fog: Korean peninsula case. *Sensors*, 19 (20):4432, 2019. doi: 10.3390/s19204432.

Sebastián Bronte, Luis Miguel Bergasa, and Pablo F. Alcantarilla. Fog detection system based on computer vision techniques. In *12th International IEEE Conference on Intelligent Transportation Systems (ITSC)*, pages 1–6, 2009. doi: 10.1109/ITSC.2009.5309842.

John Canny. A computational approach to edge detection. *IEEE Transactions on Pattern Analysis and Machine Intelligence*, 8(6):679–698, 1986. doi: 10.1109/TPAMI.1986.4767851.

Tianqi Chen and Carlos Guestrin. XGBoost: A scalable tree boosting system. *Proceedings of the 22nd ACM SIGKDD International Conference on Knowledge Discovery and Data Mining*, pages 785–794, 2016. doi: 10.1145/2939672.2939785.

Lark Kwon Choi, Jaehee You, and Alan C. Bovik. Referenceless prediction of perceptual fog density and perceptual image defogging. *IEEE Transactions on Image Processing*, 24(11):3888–3901, 2015. doi: 10.1109/TIP.2015.2456502.

Mohammad Hassan Daneshvari, Ebrahim Nourmohammadi, Mahmoud Ameri, and Barat Mojaradi. Efficient LBP-GLCM texture analysis for asphalt pavement raveling detection using eXtreme gradient boost. *Construction and Building Materials*, 401:132731, 2023. doi: 10.1016/j.conbuildmat.2023.132731.

David J. Field. Relations between the statistics of natural images and the response properties of cortical cells. *Journal of the Optical Society of America A*, 4(12):2379–2394, 1987. doi: 10.1364/JOSAA.4.002379.

Benjamin Freeston. Automated detection of features and/or parameters within an ocean environment using image data. United States Patent and Trademark Office, 2021. US Patent 10,891,481 B2, assigned to Surfline/Wavetrak, Inc.

Nicolas Hautière, Jean-Philippe Tarel, Jacques Lavenant, and Didier Aubert. Automatic fog detection and estimation of visibility distance through use of an onboard camera. *Machine Vision and Applications*, 17(1):8–20, 2006. doi: 10.1007/s00138-005-0011-1.

Kaiming He, Jian Sun, and Xiaoou Tang. Single image haze removal using dark channel prior. *IEEE Transactions on Pattern Analysis and Machine Intelligence*, 33(12):2341–2353, 2011. doi: 10.1109/TPAMI.2010.168.

Julian M. Lewis, Darko Koracin, Robert Rabin, and Jack Businger. Sea fog off the California coast: Viewed in the context of transient weather systems. *Journal of Geophysical Research: Atmospheres*, 108 (D15), 2003. doi: 10.1029/2002JD002833.

Cewu Lu, Di Lin, Jiaya Jia, and Chi-Keung Tang. Two-class weather classification. In *Proceedings of the IEEE Conference on Computer Vision and Pattern Recognition (CVPR)*, pages 3718–3725, 2014. doi: 10.1109/CVPR.2014.475.

Timo Ojala, Matti Pietikäinen, and Topi Mäenpää. Multiresolution gray-scale and rotation invariant texture classification with local binary patterns. *IEEE Transactions on Pattern Analysis and Machine Intelligence*, 24(7):971–987, 2002. doi: 10.1109/TPAMI.2002.1017623.

Said Pertuz, Domenec Puig, and Miguel Angel Garcia. Analysis of focus measure operators for shape-from-focus. *Pattern Recognition*, 46(5):1415–1432, 2013. doi: 10.1016/j.patcog.2012.11.011.

Matti Pietikäinen, Abdenour Hadid, Guoying Zhao, and Timo Ahonen. *Computer Vision Using Local Binary Patterns*. Springer, 2011. doi: 10.1007/978-0-85729-748-8.

Sonya Rauschenbach, John B. Kim, Alex W. Dye, Ian Faloona, R. Cotton Rockwood, Christopher J. Still, Kyaw Tha Paw U, and Adele L. Igel. A characterization of local spatio-temporal variability in daytime occurrence of fog along the Oregon coast using public cameras and airport weather metrics. *Agricultural and Forest Meteorology*, 388:111315, 2026. doi: 10.1016/j.agrformet.2026.111315.

Wenchen Yang, Youting Zhao, Qiang Li, Feng Zhu, and Yu Su. Multi visual feature fusion based fog visibility estimation for expressway surveillance using deep learning network. *Expert Systems with Applications*, 234:121151, 2023. doi: 10.1016/j.eswa.2023.121151.